



Enhanced thermoelectric efficiency of the bulk composites consisting of “Bi₂Te₃ matrix” and “filler Ni@NiTe₂ inclusions”

Maxim Yaprntsev^a, Alexei Vasil'ev^b, Oleg Ivanov^{a,b,*}, Marina Zhezhu^a, Ekaterina Yaprntseva^a, Vseslav Novikov^a

^a Belgorod State University, Belgorod 394015, Russian Federation

^b Belgorod State Technological University named after V.G. Shukhov, Belgorod 308012, Russian Federation

ARTICLE INFO

Article history:

Received 11 November 2020

Accepted 29 December 2020

Available online 7 January 2021

Keywords:

Thermoelectric materials

Composites

Spark plasma sintering

Microscopy and microanalysis techniques

Matrix and filler

ABSTRACT

Mixture of thermoelectric Bi₂Te₃ and ferromagnetic Ni powders was spark-plasma-sintered to prepare bulk composites with different Ni content (0.5 and 1.25 at.%). Hexagonal Bi₂Te₃, cubic Ni and trigonal NiTe₂ phases coexist in the composites. The Bi₂Te₃ phase forms matrix of the composite, whereas the Ni and NiTe₂ phases corresponds to filler. The filler is formed by Ni@NiTe₂ (“core-shell”) inclusions. Forming “core-shell” inclusions is due to high-temperature diffuse redistribution of Ni during the composites sintering. Gradient distributions of Ni, Te and Bi exist within these inclusions. Embedding the Ni filler into the Bi₂Te₃ matrix lead to drastic decrease of electrical resistivity, decrease of Seebeck coefficient, and increase of thermal conductivity. As result, the composites demonstrate enhanced thermoelectric efficiency. Optimal combination of thermoelectric properties for the composite with $x = 0.5$ at.% leads to more than two-fold enhancement of the thermoelectric figure-of-merit (~ 0.67 for the composite against ~ 0.30 for reference Bi₂Te₃ sample).

© 2020 Acta Materialia Inc. Published by Elsevier Ltd. All rights reserved.

Currently, developing the bulk micro- and nanocomposites containing a thermoelectric material as matrix with different filler inclusions is fruitful and promising way to improve thermoelectric performance of the matrix thermoelectric material [1–5]. Several mechanisms can simultaneously be involved to vary the thermoelectric properties (specific electrical resistivity, ρ , Seebeck coefficient, S , and thermal conductivity, k) of the composite. In turn, these properties govern the thermoelectric figure-of-merit, $ZT = (S^2/\rho)kT$, where T is absolute temperature. The inclusions themselves can act as scattering centers for electrons and phonons affecting ρ and k , respectively, whereas matrix/filler interfaces can result in S increase via electron energy filtration effect [6,7]. Resulted enhancing in ZT of the bulk thermoelectric composites is crucially dependent on material, size and concentration of the filler inclusions. Applying the metallic inclusions possessing ferro- or antiferromagnetic ordering allows implementing new thermoelectromagnetic effects, which can additionally improve the thermoelectric properties of the bulk composites [8,9]. These effects are as follows: (i) scattering of carriers by magnetic moments of the filler inclusions (similar to the Kondo effect) leading to decrease of electron mobility; (ii) increase of electron concentration due to rectifying properties of metal-semiconductor contact corre-

sponding to matrix/filler interface affecting ρ ; (iii) localization of electrons near matrix/filler interface leading to decrease of their mobility and formation of magnetic polarons; (iv) entrainment effect of carriers by paramagnons (paramagnon drag) affecting ρ , k and S , too.

The aim of present work is to prepare the bulk composites consisting of “thermoelectric Bi₂Te₃ matrix” and “ferromagnetic Ni filler”, and to find and analyze features in both the microstructure and the thermoelectric properties of the composites. The matrix material is used as one of end members to prepare two-component n -Bi₂Te_{3-x}Se_x and p -Bi_{2-x}Sb_xTe₃ alloys for low-temperature thermoelectric applications [10,11]. The filler material is ferromagnet with the Curie temperature at 628 K [12].

To prepare the composites with different Ni content, x ($x = 0.5$ and 1.25 at.%), individual Bi₂Te₃ and Ni powders were preliminary synthesized. To synthesize the Bi₂Te₃ powder, high pure Bi₂O₃, SeO₂, TeO₂ precursors taken in stoichiometric ratio were dissolved in ethylene glycol with some addition of alkaline agent (KOH) to control pH-value. The obtained solution was transferred to round-bottom flask and heated to boiling point. After evaporation of water impurity, the flask with solution sealed with reflux and maintained at 458 K for 4 h. The resulted dark suspension was cooled to room temperature. The powder was purified by filtration and washing for 3 times with ethanol and acetone. Finally, the powder was dried in argon atmosphere at 523 K for 2 h. To synthesize the

* Corresponding author.

E-mail address: Ivanov.Oleg@bsu.edu.ru (O. Ivanov).

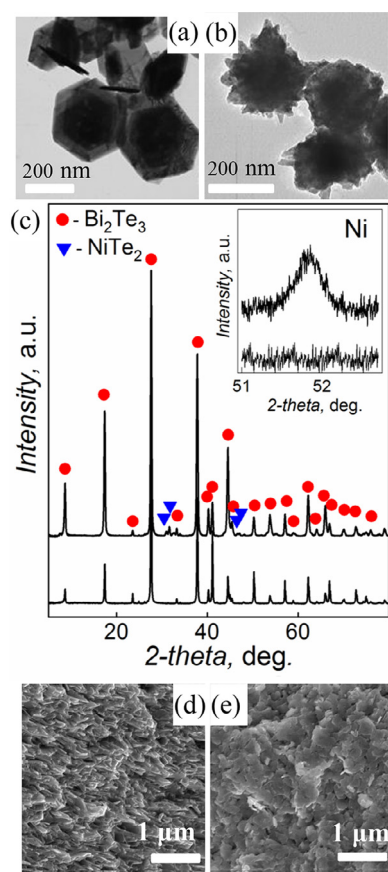


Fig. 1. Upper panel: TEM images of the Ni (a) and Bi₂Te₃ (b) powders. Middle panel: XRD patterns for the composite with $x = 1.25$ at.% (upper pattern) and mixture of the Bi₂Te₃ and Ni powders of the same composition (lower pattern); inset: enlarged part of XRD pattern for the composite, which corresponds to the Ni phase. Bottom panel: SEM images taken on fractured surfaces perpendicular (a) and parallel (b) to SPS-pressing direction.

Ni powder, 5 g Ni(NO₃)₂·6H₂O was firstly dissolved in 400 ml ethylene glycol. Subsequently, 10 g KOH was added into the solution. The mixture was heated to 353 K under vigorously stirring to homogeneity. Then, the resulted sol was cooled to room temperature. Hydrazine hydrate was slowly added follow. The reaction mixture was heated to 373 K and maintained to 1 h to complete reduction process from Ni²⁺ to Ni⁰. The obtained powder was collected by neodymium magnet and washed with ethanol and acetone to remove organic impurities.

According to X-ray diffraction (XRD) analysis, carried out by Rigaku Ultima IV diffractometer with CuK_α – radiation, the Bi₂Te₃ powder was single hexagonal $R\bar{3}m$ phase with lattice a and c parameters equal to 0.4354 and 0.3035 nm, respectively, and the Ni powder was single face-centered $Fm\bar{3}m$ cubic phase with $a = 0.3525$ nm. According to transmission electron microscopy (TEM) examination, carried out by model JEM - 2100 microscope, the Bi₂Te₃ powder mainly consisted of hexagonal plate-shaped particles with sizes of $\sim 300 \div 500$ nm (Fig. 1(a)), whereas the Ni powder mainly consisted of irregularly shaped agglomerated formations with sizes of $150 \div 200$ nm (Fig. 1(b)). Agglomerating many Ni particles can be related to ferromagnetic interaction between the particles.

To prepare the bulk composites, the Bi₂Te₃ and Ni powders, taken in stoichiometric ratio for different x , were thoroughly mixed by a planetary mill for 30 min. The mixed Bi₂Te₃ + Ni powders were spark-plasma-sintered (SPS) at pressure of 40 MPa and temperature of 573 K for 2 min in vacuum. Phase composition of the

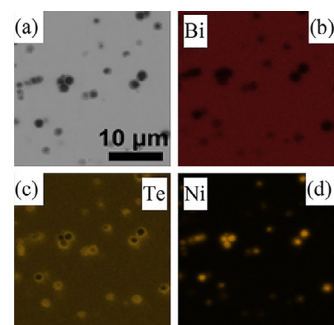


Fig. 2. BSE image of polished surface (a), and maps of Bi (b), Te (c) and Ni (d) distributions for the composite with $x = 1.25$ at.%.

bulk composites was found to be changed during SPS-process. Besides the initial Bi₂Te₃ and Ni phases, a new NiTe₂ phase was observed. This phase corresponds to trigonal $P\bar{3}m1$ structure with lattice a and c parameters equal to 0.3895 and 0.5470 nm, respectively. For instance, coexistence of three phases for the composite with $x = 1.25$ at.% is confirmed by upper XRD pattern shown in Fig. 1(c). The pattern was taken from surface, oriented perpendicularly to SPS-pressing direction. Lower XRD pattern corresponds to mixture of the Bi₂Te₃ and Ni powders, which was used to prepare the relevant bulk composite. Additional peaks of the NiTe₂ phase, indicated by triangles, appear in XRD pattern of the composite. Due to small Ni content, these peaks are expressed very weakly as shown in inset to Fig. 1(c).

It is known that SPS-process is usually resulting in texturing of compounds based on Bi₂Te₃, and a texturing axis coincides with SPS-pressing direction [13–16]. The texturing is observed in SEM images of grain structures, which are recorded on fractured surfaces, oriented parallel and perpendicularly to SPS-pressing direction. SEM images taken for the composite with $x = 1.25$ at.% are presented in bottom panel of Fig. 1. At surface parallel to SPS-pressing direction, lamellar structure is formed (Fig. 1(d)), and lamellar sheets consist of grains, which are elongated in plane, oriented perpendicularly to this direction. At surface perpendicular to SPS-pressing direction, disordered grain structure with grains having mainly irregular shape is observed (Fig. 1(e)). Average lateral size and thickness of grains were equal to ~ 500 and 50 nm, respectively.

Coexistence of the Bi₂Te₃, Ni and NiTe₂ phases can be confirmed by analysis of backscattered electron (BSE) image, and mapping of Bi, Te and Ni distribution per surface of the composite, carried out by energy dispersive X-ray spectroscopy (EDS) method. A Nova NanoSEM 450 microscope was applied for these experiments. BSE image taken for polished surface of the composite with $x = 1.2$ at.% is shown in Fig. 2(a). Three different phases can be found in this Fig. According to Bi, Te and Ni maps (Figs. 2(b), (c) and (d)) and taking into account results of XRD analysis (Fig. 1(c)), major phase should be attributed to the matrix Bi₂Te₃ phase, whereas minor Ni and NiTe₂ phases form the filler inclusions. These inclusions are, firstly, dominantly circle-shaped, and, secondly, consist of a Ni core covered with a NiTe₂ shell, i.e. the Ni@NiTe₂ inclusions are naturally formed in the composite being studied. Forming the filler Ni@NiTe₂ inclusions can be originated from high-temperature diffusion redistribution of Ni, which occurs during SPS-process. Actually, before starting SPS-process, initial Ni inclusions can be considered as impurity Ni sources, which are randomly distributed inside the Bi₂Te₃ matrix. So, an initial Ni distribution will be strongly inhomogeneous. During high-temperature SPS-process, Ni is starting to diffuse from the initial inclusions (the impurity Ni sources) into the Bi₂Te₃ matrix with trend to form a homogeneous Ni distribution. Due to the diffuse Ni redistribution and chemical inter-

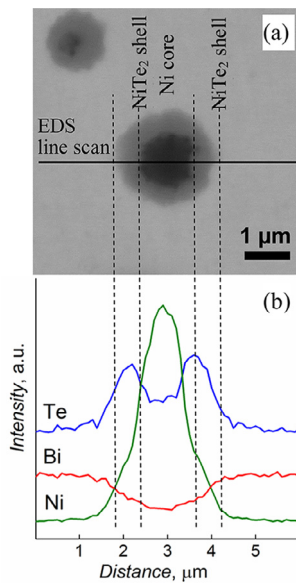


Fig. 3. BSE image of the filler Ni@NiTe₂ inclusion (a), and EDS line scan profiles of Te, Bi and Ni taken along line crossing the inclusion (b).

action between Bi₂Te₃ and Ni, new NiTe₂ phase can be formed as the shell surrounding the Ni core.

BSE image of a separate filler Ni@NiTe₂ inclusion is shown in Fig. 3(a). EDS line scan profiles of Te, Bi and Ni taken along line crossing the inclusion is also shown in Fig. 3(b). According to EDS line scan analysis, Ni is dominantly containing inside the core, whereas Ni, and Te are dominated inside the shell. Far from the inclusion, Te and Bi are homogeneously distributed, and Ni is missing. For the inclusion, which is shown in Fig. 3(a), thickness of the shell, d , and radius of the core, r , are approximately equal to each other ($\sim 1 \mu\text{m}$). Besides the inclusions with equal d and r , other types of the inclusions can be also observed in Fig. 2(a). Ones of these inclusions consist of very small cores, but large shells, i.e. $d > (\text{or } \gg) r$ is for these inclusions. The inclusion of this type can be found in upper-left corner of Fig. 3(a). Unlike the inclusions with dominated shells, the inclusions with dominated cores, $r > (\text{or } \gg) d$ can be also observed.

A ratio between $d > (\text{or } \gg) r$ for the Ni@NiTe₂ inclusions is obviously dependent on initial size of the Ni agglomerations in the starting Ni powder, which is applied to sinter the bulk composite. For the small-sized agglomerations, holding time and temperature of SPS-process are enough to almost all Ni filler was dissolved inside the Bi₂Te₃ matrix and formed the NiTe₂ phase. For the large-sized agglomerations, only small fraction of the Ni filler has time to diffuse inside the matrix and, hence, thin enough NiTe₂ shell surrounding big Ni core is formed in this case. Finally, for the middle-sized agglomerations, the Ni@NiTe₂ inclusions with almost equal d and r are formed. Since there are gradient distributions of elements within these inclusions, they can be called as locally-gradient domains. Then, the composite containing these locally-gradient domains should be considered as locally-gradient composites.

To study the thermoelectric properties of the composites, the $2 \times 2 \times 10 \text{ mm}$ bars and the $\emptyset 10 \times 2 \text{ mm}$ disks were prepared. The specific electrical resistivity and the Seebeck coefficient of the bar samples were measured by using ZEM-3 system. The total thermal conductivity of the disk-shaped samples was measured by TC-1200 system using a laser flash method. To extract any changes in the thermoelectric properties of the matrix Bi₂Te₃ thermoelectric due to embedding the filler inclusions, pure Bi₂Te₃ compound non containing the filler ($x=0$) was also prepared using the technological scheme and parameters that was used to prepare the bulk compos-

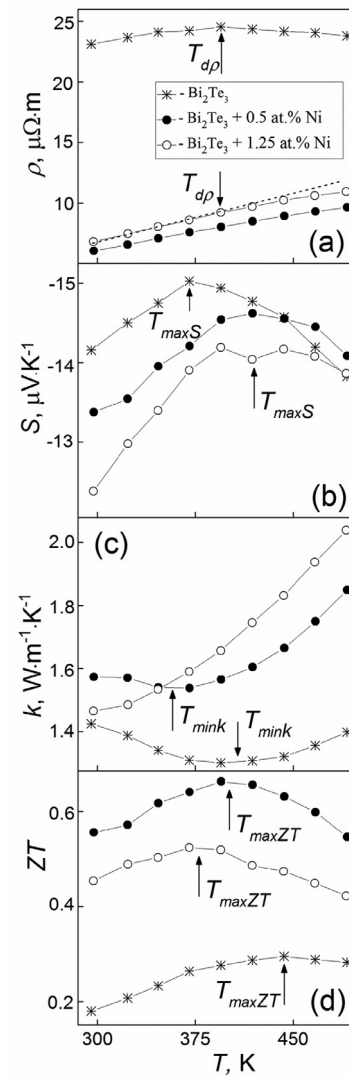


Fig. 4. Temperature dependences of ρ (a), S (b), k (c) and ZT (d) for the reference Bi₂Te₃ material and the bulk composites $x=0.5$ and 1.25 at.%.

ites. This compound will be further used as a reference sample. It is known that for the textured samples, the thermoelectric properties, measured parallel or perpendicularly to the texturing axis, are happening to be quite different [13]. Better properties are corresponding to the perpendicular measuring direction. Hence, only these properties are analyzed here. Temperature dependence of ρ , S , k and ZT taken for the bulk composites and reference sample are shown in Figs. 4(a), (b), (c) and (d), respectively. A few features can be found in these dependences. With increasing temperature, ρ is steady increasing up to temperature $T_{d\rho} \approx 375 \text{ K}$ (Fig. 4(a)). But at $T_{d\rho}$, the maximum (for the reference sample) or kinks (for the bulk composites) are appeared in the $\rho(T)$ dependences. Below $T_{d\rho}$, the $\rho(T)$ behavior corresponds to regime of degenerate semiconductor [17,18]. In this case, electron concentration is T -independent, and the $\rho(T)$ behavior is mainly governed by temperature behavior of electron mobility. Above $T_{d\rho}$, onset of intrinsic conductivity due to a thermal excitation of carriers from valence band to conduction band takes place. Embedding the Ni filler into the Bi₂Te₃ matrix results in drastic decrease of ρ , but the $\rho(T)$ curves for two composites are positioned very close to each other. The filler inclusions usually act as scattering centers for electrons, resulting in reducing their mobility. Then, decrease of ρ , observed for the com-

posites, should be attributed to increase of electron concentration. The intrinsic conductivity is also affecting the $S(T)$ dependences (Fig. 4(b)). All the $S(T)$ curves are bell-like shaped that is related to bipolar effect, which is typical for doped Bi_2Te_3 and Bi_2Te_3 -based compounds [17–20]. Besides, sign of S is negative that is in agreement with n -type conductivity of the samples studied. The bipolar effect is observed, when electrons and holes are simultaneously present in solid. The thermal excitation of carriers due to the intrinsic conductivity does not change the majority carriers concentration too much, whereas the minority carriers concentration is remarkably increasing. Sign of S for n -type conductivity is negative, whereas p -type conductivity is characterized by positive sign of S . As result, competition of two S contributions with opposite signs results in forming the $S(T)$ maxima in the $S(T)$ curves. This maximum is positioned at $T_{\max S} \approx 375\text{ K}$ for the reference sample, and with increasing x , it is shifting to higher temperatures. Besides, S for the composites is lower as compared to that for the reference sample. This feature can also be related to increase of electron concentration due to embedding the Ni filler into the Bi_2Te_3 matrix. Onset of the intrinsic conductivity is reflected in temperature behavior of k , too (Fig. 4(c)). This behavior is rather complicated and combined by contributions of lattice thermal conductivity, electron thermal conductivity and bipolar thermal conductivity. Growth of k , which is observed above $T_{\min k}$ for the reference sample and the composite with $x = 0.5$ at.%, is originated from the bipolar thermal conductivity [21]. For the composite with $x = 1.25$ at.%, $T_{\min k}$ is positioned at or below room temperature. The lowest k is observed for the reference sample. In accordance with change of ρ (Fig. 4(a)), increase of k for the composites can be related to increase of electron thermal conductivity via relevant increase of electron concentration.

Finally, the $\rho(T)$, $S(T)$, and $k(T)$ dependences were used to plot the temperature dependences of ZT (Fig. 4(d)). All the $ZT(T)$ curves have the maxima centered at temperatures $T_{\min ZT}$. The $T_{\min ZT}$ is dependent on composition of the samples studied. For the reference sample and the composites with $x = 0.5$ and 1.25 at.%, the maxima are positioned at ~ 440 , ~ 400 and $\sim 375\text{ K}$, respectively. These maxima are related to onset of the intrinsic conductivity, which is harmful for the thermoelectric efficiency enhancement, since thermal excitation of electron-hole pairs reduces the Seebeck coefficient and increases the thermal conductivity. ZT for the composites is higher as compared to that for the reference sample. Embedding the Ni filler into the Bi_2Te_3 matrix leads to decrease of ρ and S , and increase of k . Decrease of ρ is the strongest effect. Optimal combination of ρ , S and k for the composite with $x = 1.25$ at.% results in more than two-fold enhancement of ZT (~ 0.67 for the composite against ~ 0.30 for the reference sample).

Thus, the composites consisting of “ Bi_2Te_3 matrix” and “filler

Ni@NiTe_2 inclusions” really possess the enhanced thermoelectric efficiency. At present, to correctly find the physical mechanisms, responsible for changes of the thermoelectric properties of the composites, experimental work is in progress. However, according to preliminary results, enhancing the thermoelectric figure-of-merit can probably be related to increase of electron concentration. In turn, for the composites with the metallic inclusions, this increase of electron concentration can be due to rectifying properties of metal-semiconductor contact corresponding to matrix/filler interface.

This work was supported by the Ministry of Science and Higher Education of the Russian Federation (grant number No 0625–2020–0015). All of studies were carried out by the scientific equipment of joint research center “Technologies and Materials” at the Belgorod State University.

Declaration of Competing Interest

The authors declare that they have no known financial interests or personal relationship that could have appeared to influence the work reported in this paper.

References

- [1] O. Ivanov, O. Maradudina, R. Lyubushkin, J. Alloys Compd. 586 (2014) 679.
- [2] Y.-X. Yang, Y.-H. Wu, Q. Zhang, G.-S. Cao, T.-J. Zhu, X.-B. Zhao, Rare Metals 39 (2020) 5895.
- [3] W.-K. Yan, A.-B. Zhang, L.-J. Yi, B.-L. Wang, J. Wang, Chin. Phys. B. 29 (2020) 057301.
- [4] M.G. Kanatzidis, Chem. Mater. 22 (2009) 648.
- [5] W. Liu, X. Yan, G. Chen, Z. Ren, Nano Energy 1 (2012) 42.
- [6] J.H. Bahk, Z. Bian, A. Shakouri, Phys. Rev. B. 89 (2014) 075204.
- [7] J.H. Bahk, Z. Bian, A. Shakouri, Phys. Rev. B. 87 (2013) 075204.
- [8] W. Zhao, Z. Liu, P. Wei, Q. Zhang, W. Zhu, X. Su, X. Tang, J. Yang, Y. Liu, J. Shi, Y. Chao, S. Lin, Y. Pei, Nat. Nanotech. 12 (2017) 55.
- [9] W. Zhao, Z. Liu, Z. Sun, Q. Zhang, P. Wei, X. Mu, H. Zhou, C. Li, S. Ma, D. He, P. Ji, W. Zhu, X. Nie, X. Su, X. Tang, B. Shen, X. Dong, J. Yang, Y. Liu, J. Shi, Nature 549 (2019) 247.
- [10] H.J. Goldsmid, Materials (Basel) 7 (2014) 2577.
- [11] G.S. Nolas, J. Sharp, H.J. Goldsmid, Thermoelectrics Basic Principles and New Materials Developments, Springer, Berlin, 2001.
- [12] B.D. Cullity, C.D. Graham, Introduction to Magnetic Materials, Piscataway, IEEE Press, 2009.
- [13] O. Ivanov, M. Yaprıntsev, A. Vasil'ev, J. Sol. St. Chem. 290 (2020) 121559.
- [14] A. Vasil'ev, M. Yaprıntsev, O. Ivanov, E. Danshina, Sol. St. Sci. 84 (2018) 28.
- [15] Q. Lognon, F. Gascoin, O.I. Lebedev, L. Lutterotti, S. Gascoin, D. Chateigner, J. Am. Ceram. Soc. 97 (2014) 2038.
- [16] S.D. Bhame, D. Pravarthana, W. Prellier, J.G. Noudem, Appl. Phys. Lett. 102 (2013) 2190.
- [17] O. Ivanov, M. Yaprıntsev, R. Lyubushkin, O. Soklakova, Scr. Mater. 146 (2018) 91.
- [18] M. Yaprıntsev, R. Lyubushkin, O. Soklakova, O. Ivanov, J. Electron. Mater. 47 (2018) 1362.
- [19] J. Yang, F. Wu, Z. Zhu, L. Yao, H. Song, X. Hu, J. Alloys Compd. 619 (2015) 401.
- [20] F. Wu, H. Song, J. Jia, X. Hu, Prog. Nat. Sci. Mater. Int. 23 (2013) 408.
- [21] S. Wang, J. Yang, T. Toll, J. Yang, W. Zhang, X. Tang, Sci. Rep. 5 (2015) 10136.